






Article

Chemical and Structural Changes by Gold Addition Using Recharge Method in NiW/Al₂O₃-CeO₂-TiO₂ Nanomaterials

Jorge Cortez-Elizalde ¹, Ignacio Cuauhtémoc-López ¹, Zenaida Guerra-Que ², Alejandra Elvira Espinosa de los Monteros ¹, Ma. Antonia Lunagómez-Rocha ¹, Adib Abiu Silahua-Pavón ¹, Juan Carlos Arévalo-Pérez ¹, Adrián Cordero-García ¹, Adrián Cervantes-Urbe ¹ and José Gilberto Torres-Torres ^{1,*}

- ¹ Laboratorio de Nanomateriales Catalíticos Aplicados al Desarrollo de Fuentes de Energía y Remediación Ambiental, Centro de Investigación de Ciencia y Tecnología Aplicada de Tabasco (CICTAT), Universidad Juárez Autónoma de Tabasco, DACB, Km.1 Carretera Cunduacán-Jalpa de Méndez, Cunduacán 86690, Tabasco, Mexico; LINK-190@hotmail.com (J.C.-E.); nachoftir@gmail.com (I.C.-L.); ale2962@gmail.com (A.E.E.d.l.M.); manlura9@hotmail.com (M.A.L.-R.); adibab45@gmail.com (A.A.S.-P.); carlos.arevalo@ujat.mx (J.C.A.-P.); adrian.cordero@ujat.mx (A.C.-G.); adrian.cervantes@ujat.mx (A.C.-U.)
- ² Laboratorio de Investigación 1 Área de Nano-Tecnología, Tecnológico Nacional de México Campus Villahermosa, Km. 3.5 Carretera Villahermosa-Frontera, Cd. Industrial, Villahermosa 86010, Tabasco, Mexico; zenaida.gq@villahermosa.tecnm.mx
- * Correspondence: gilberto.torres@ujat.mx; Tel.: +52-19143360928



Citation: Cortez-Elizalde, J.; Cuauhtémoc-López, I.; Guerra-Que, Z.; Espinosa de los Monteros, A.E.; Lunagómez-Rocha, M.A.; Silahua-Pavón, A.A.; Arévalo-Pérez, J.C.; Cordero-García, A.; Cervantes-Urbe, A.; Torres-Torres, J.G. Chemical and Structural Changes by Gold Addition Using Recharge Method in NiW/Al₂O₃-CeO₂-TiO₂ Nanomaterials. *Materials* **2021**, *14*, 5470. <https://doi.org/10.3390/ma14195470>

Academic Editors: Vlassios Likodimos and Maria Harja

Received: 28 June 2021

Accepted: 15 September 2021

Published: 22 September 2021

Publisher's Note: MDPI stays neutral with regard to jurisdictional claims in published maps and institutional affiliations.



Copyright: © 2021 by the authors. Licensee MDPI, Basel, Switzerland. This article is an open access article distributed under the terms and conditions of the Creative Commons Attribution (CC BY) license (<https://creativecommons.org/licenses/by/4.0/>).

Abstract: NiWAu trimetallic nanoparticles (NPs) on the surface of support Al₂O₃-CeO₂-TiO₂ were synthesized by a three-step synthetic method in which Au NPs were incorporated into presynthesized NiW/Al₂O₃-CeO₂-TiO₂. The recharge method, also known as the redox method, was used to add 2.5 wt% gold. The Al₂O₃-CeO₂-TiO₂ support was made by a sol-gel method with two different compositions, and then two metals were simultaneously loaded (5 wt% nickel and 2.5 wt% tungsten) by two different methods, incipient wet impregnation and ultrasound impregnation method. In this paper, we study the effect of Au addition using the recharge method on NiW nanomaterials supported on mixed oxides on the physicochemical properties of synthesized nanomaterials. The prepared nanomaterials were characterized by scanning electron microscopy, BET specific surface area, X-ray diffraction, diffuse reflectance spectroscopy in the UV-visible range and temperature-programmed desorption of hydrogen. The experimental results showed that after loading of gold, the dispersion was higher (46% and 50%) with the trimetallic nanomaterials synthesized by incipient wet impregnation plus recharge method than with impregnation plus ultrasound recharge method, indicating a greater number of active trimetallic (NiWAu) sites in these materials. Small-sized Au from NiWAu/ACTU1 trimetallic nanostructures was enlarged for NiWAu/ACT1. The strong metal NPs-support interaction shown for the formation of NiAl₂O₄, Ni-W-O and Ni-Au-O species simultaneously present in the surface of trimetallic nanomaterial probably plays an important role in the degree of dispersion of the gold active phase.

Keywords: gold addition; recharge method; NiW/Al₂O₃-CeO₂-TiO₂ nanomaterials

1. Introduction

Supported bimetallic nanoparticles (NPs) alloys or even recently trimetallic NPs have been a strategy commonly used in nanomaterials reports [1–8]. It is well known that the nanostructured nanomaterials must be designed with high stability against leaching and agglomeration or sintering.

The addition of second metal in the bimetallic system significantly enhances the stability and the activity of the designed catalysts due to a synergistic interaction [9]. Moreover, indeed, the addition of a third metallic component improves the stability of a second metal in a parent bimetallic system [6,10–12]. Jin et al. [10] found the enhanced

stability of trimetallic alloy material (Ni-Fe-Cu) during dry reforming of methane (DRM) and weakened leaching of Fe. The Fe was affected by the reaction conditions of this application in the bimetallic system.

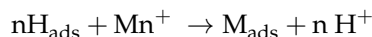
The preparation methods can synthesize supported NPs in a single step or in two steps. In the case of a single step, both the precursor salt of the support and the active phase are added in the reaction mixture; otherwise, in sequential or two-step, first the support is synthesized, usually an oxide, and then the active phase, usually a metal, is prepared by some other specific method, expecting all the metal to be added and adsorbed on the support, without metal loss and with a high metal dispersion. The methods mentioned above for the nanostructure NPs depend on many factors such as the pH value, the calcination temperature, metal loading, nature of support and metal or metals, which have significant consequences on the catalytic properties of the NPs. These methods determine important properties such as homogeneous metal dispersion, high specific surface area, adequate acidity/basicity ratio, metal–support interaction, metal–metal interaction, metal–metal–metal interaction and generation of structural defects such as oxygen vacancies and reducibility [13–17].

Indeed, Mendoza-Nieto et al. [18] studied NiMoW trimetallic catalysts supported on SBA-15 and conventional γ -Al₂O₃ support in hydrodesulfurization (HDS), and they found an effect of used support on the catalytic behavior of HDS. They explained this effect by the strong metal–support (Al₂O₃) interaction due to the presence of a significant amount (75%) of Mo⁶⁺ and W⁶⁺ species in tetrahedral coordination and the weak interaction with the deposited metal species on SBA-15 due to the formation of agglomerated NiMoO₄ and/or WO₃ species in the catalyst and larger proportion of octahedrally coordinated metal species. Jahel et al. [19] demonstrated that the indium addition at higher loadings in trimetallic Pt/Al₂O₃SnIn–Cl naphtha-reforming catalyst decreases the acidity of the support and increases isomerization selectivity. Bocanegra et al. [20] synthesized InPtSn trimetallic NPs with different Sn contents supported on MgAl₂O₄. They concluded that trimetallic catalysts displayed a strong interaction between the different metals, which could be responsible for the good performance of these systems in catalytic dehydrogenation. The total acidity of the Pt–Ir–Ge trimetallic catalyst was slightly increased after Ge addition, as reported by Samoila et al. [21]. Liang et al. [22] synthesized highly dispersed non-noble trimetallic Cu–Ni–Co NPs supported on the pores of the metal–organic framework MIL-101, and they attributed the enhancement in the catalytic performance of the hydrolysis of ammonia borane to the large catalyst surface as well as the synergetic effect between trimetallic NPs.

Gold in small particles (<5nm) supported on oxides could be active even at ambient temperature. The nanometric gold synthesized has shown a relationship between the kind of support that has been used and the catalytic activity of the nanometal [23–25]. In addition to the classic deposition–precipitation method (DP) proposed by Haruta et al. [26], different methods have been developed to prepare highly active Au catalysts [27–36]. Normally, these preparation methods can produce small gold particles (<10 nm) that are strongly linked to the support; most of them require total control of synthesis parameters due to the strong influence of the preparation conditions on the final characteristics of the material and therefore on its catalytic properties.

A three-step synthetic method was selected for the present study. First, Al₂O₃-CeO₂-TiO₂ support was prepared by a sol–gel method with two different compositions, and then two metals were simultaneously loaded (5% nickel and 2.5% tungsten) by two different methods, incipient wet impregnation and ultrasound impregnation method. For the final step, for the formation of supported Au/NiW trimetallic NPs, we used the recharge method, also known as the redox method. The recharge method favors the deposit of the second metal on the first prerduced metal in order to create metal–metal interactions. A group of researchers from the University of Poitiers led by Professor Barbier [37] named it the redox method or recharge method, in which surface reactions modify the catalyst between

chemisorbed hydrogen over the first metal and the cation of the second metal according to the following scheme:



where H_{ads} is the adsorbed hydrogen over the metal surface, Mn^+ is the cation of the second metal in solution and M_{ads} is the second adsorbed metal.

The preparation strategy used in this study was developed in order to generate small trimetallic NPs and to favor strong metal–support interaction and strong metal–metal–metal interaction. The aim of this work was to disperse gold NPs below 5 nm into the mixed oxide Al_2O_3 - CeO_2 - TiO_2 prepared by sol–gel method modified with Ni and W to study the effect that Au nanoparticles have on the physicochemical properties of these trimetallic NPs materials due to intimate contact between three metal constituents in the catalyst nanostructure.

2. Materials and Methods

2.1. Materials Preparation

The Al_2O_3 - CeO_2 - TiO_2 supports were prepared via the sol–gel method; these were prepared varying weight percentages of aluminum, cerium and titanium oxide (90 wt% Al_2O_3 , 1 wt% CeO_2 and 9 wt% TiO_2 named ACT1 and 94 wt% Al_2O_3 , 1 wt% CeO_2 and 5 wt% TiO_2 named ACT2). The metallic precursors used were aluminum tri-sec-butoxide $\text{Al}[\text{OCH}(\text{CH}_3)\text{C}_2\text{H}_5]_3$ (97% Aldrich), titanium butoxide (IV) $\text{Ti}[\text{O}(\text{CH}_2)_3\text{CH}_3]_4$ (97% Aldrich), cerium nitrate (III) hexahydrate $\text{Ce}(\text{NO}_3)_3$ (99.999% Aldrich) and a mixture of water and n-butanol (99.9%, Baker), in relation to alkoxide/butanol 1:8 in volume and alkoxide/water 1:16 in volume. They were aged at 70 °C for 24 h and dried in a rotary evaporator; finally, the samples were calcined at 550 °C for 12 h using a heating ramp of 2 °C/min.

The four bimetallic supported catalysts were obtained by the wet impregnation method and the ultrasound method. The incorporation of the active metal phase on Al_2O_3 - CeO_2 - TiO_2 support was conducted to obtain a nominal 5 wt% Ni and 2.5 wt% W loading.

Deposition of Ni and W into the modified supports was carried out by the wet impregnation method according to the following procedure: First, 5 wt% Ni and 2.5 wt% W were loaded in 10 g of support, and 100 mL of the precursor salt of $\text{Ni}(\text{NO}_3)_2 \cdot 6\text{H}_2\text{O}$ (Sigma-Aldrich) and hydrated ammonium metatungstate $(\text{NH}_4)_6\text{H}_2\text{W}_{12}\text{O}_{40} \cdot \text{XH}_2\text{O}$ (85%, Aldrich Chemistry) was used to synthesize the active phases and metal promoters. They were subjected to a calcination process at 2 °C/min in airflow/ O_2 at 400 °C; subsequently, they were reduced in H_2 flow at 400 °C for 4 h.

The ultrasound method was used to impregnate 5 wt% Ni and 2.5 wt% W in 5 g of support in 50 mL of water under vibration in ultrasound (8890–Cole Parmer); the prepared materials were dried in a rotary evaporator and then dried in an oven at 120 °C for 12 h. Afterward, they were calcined using a heating ramp of 2 °C/min in airflow/ O_2 at 400 °C for 4 h. Finally, they were reduced in H_2 flow at 400 °C for 4 h using the same heating ramp as for the calcination.

The recharge method was used to impregnate the supported bimetallic Ni-W NPs with 2.5 wt% Au, applying hydrated tetrachloroauric acid as a precursor ($\text{HAuCl}_4 \cdot 3\text{H}_2\text{O}$). The amount of bimetallic NPs needed to prepare 2 g of trimetallic NPs was introduced into the quartz reactor. First, the NiW/ Al_2O_3 - CeO_2 - TiO_2 bimetallic catalyst was reduced with hydrogen at a temperature of 400 °C, and then 5 mL of the solution HCl was added at 0.2 M. Then, a gold solution $\text{HAuCl}_4 \cdot 3\text{H}_2\text{O}$ was introduced at 2.5 wt%. Finally, the nanocatalysts were activated by reduction of hydrogen at a temperature of 400 °C for 4 h using the same heating ramp of the above-mentioned heat treatments. Figure 1 shows the system used to prepare the materials by the recharge method. The Table 1 shows the materials prepared, their compositions, their metal loads, the preparation method and the code assigned.

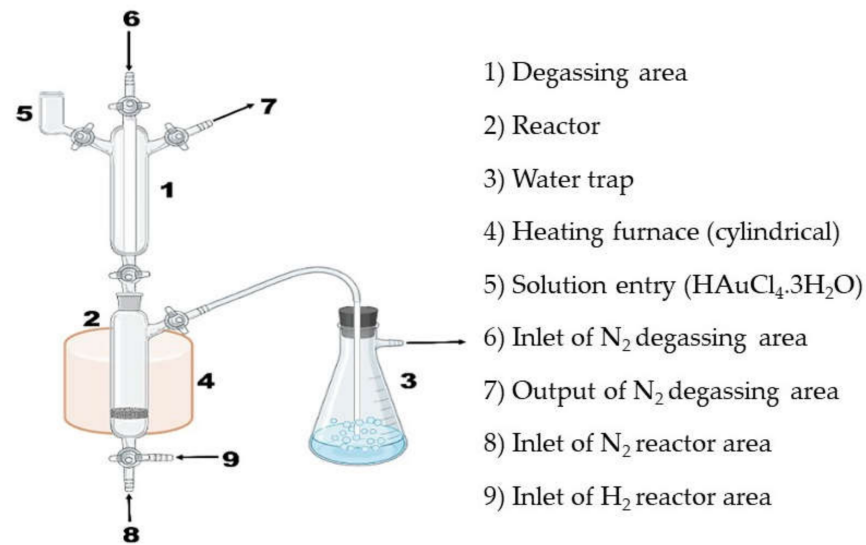


Figure 1. Synthesis system for the preparation of NiWAu/Al₂O₃-CeO₂-TiO₂ nanomaterials by recharge method.

Table 1. Nanomaterials synthesized by the wet impregnation, ultrasound and recharge method.

Method	Weight Percentage		Material	Code
	Nickel (Ni)	Tungsten (W)		
Wet impregnation	5%	2.5%	NiW/Al ₂ O ₃ -CeO ₂ -TiO ₂ 90% 1% 9%	NiW/ACT1
			NiW/Al ₂ O ₃ -CeO ₂ -TiO ₂ 94% 1% 5%	NiW/ACT2
Ultrasound impregnation	5%	2.5%	NiW/Al ₂ O ₃ -CeO ₂ -TiO ₂ 90% 1% 9%	NiW/ACTU1
			NiW/Al ₂ O ₃ -CeO ₂ -TiO ₂ 94% 1% 5%	NiW/ACTU2
Recharge	Gold (Au)	2.5%	NiWAu/ACT1	NiWAu/ACTU1
			NiWAu/ACT2	NiWAu/ACTU2

2.2. Materials Characterization

2.2.1. X-ray Diffraction

The equipment used was a Bruker AXS model D8 Advance diffractometer (Borchen, North Rhine-Westphalia, Germany). A Cu anode was used; the radiation corresponded to the transition CuK α with a wavelength of 1.5418 Å from 20 to 80° in the scale of 2 θ , with a step size of 0.02° and a time per step of 1 s.

2.2.2. UV-Vis Diffuse Reflectance Spectroscopy (UV-Vis DRS)

The diffuse reflectance spectra of the synthesized nanomaterials were obtained with a UV-Vis Varian Cary 300 spectrophotometer (Varian Inc., Palo Alto, CA, USA), provided with an integration sphere, useful for the powder analysis. The 190–800 nm region was analyzed using BaSO₄ as a white reflectance standard to obtain the baseline.

2.2.3. BET Specific Surface Area (SSA)

The textural property characterization of the supports and bimetallic and trimetallic nanomaterials was carried out by physical adsorption of N₂ (Praxair 5.0 U.A.P.) at −198 °C using a Micromeritics Model TriStar II (Micromeritics Instrument Corporation 4356 Communications Drive, Norcross, GA, USA). BET specific surface area determinations were performed using the Brunauer, Emmett and Teller (BET) method; pore volume (V_p) and

pore size distribution (PSD) were assessed by the BJH method. Prior to nitrogen adsorption analysis, the samples were degassed under nitrogen flow at 150 °C overnight.

2.2.4. Scanning Electron Microscopy (SEM)

Energy dispersive X-ray spectroscopy (EDX) coupled with scanning electron microscopy (SEM) was used to appreciate the morphology, and semiquantitative analysis was performed with the BES detector of particles corresponding to the materials synthesized in a JEOL brand model JSM-6010LA (Jeol Ltd, Akishima Tokyo, Japan).

2.2.5. Transmission Electron Microscopy (TEM)

Transmission electron microscopy (TEM) was performed with a JEOL JEM2100 STEM (Jeol Ltd, Akishima Tokyo, Japan). The samples were ground, suspended in ethanol at room temperature and dispersed with agitation in an ultrasonic bath for 15 min; then, an aliquot of the solution was passed through a carbon copper grid. The particle size distribution of the catalysts was obtained by measuring more than 200 nanoparticles in each sample.

The particle average diameter (d_m) was calculated using the formula:

$$d_m = \frac{\sum_i (x_i d_i)}{\sum_i x_i} \quad (1)$$

where x_i is the number of particles with diameter d_i .

2.2.6. Temperature-Programmed Desorption of Hydrogen (TPD-H₂)

This characterization technique used an automated chemisorption analyzer, model Belcat B (Bel-Japan) with thermal conductivity detector, using 0.2 g of catalyst. First, the samples were pretreated with the following protocol: 20% O₂/H₂ for 30 min at 400 °C, 20% O₂/H₂ for 1 min at 35 °C, He for 60 min at 35 °C, 5% H₂/Ar for 30 min at 400 °C, 5% H₂/Ar for 1 min at 35 °C with a flow rate of 50 sccm. Then, the samples were treated with Ar at 50 sccm. The temperature was raised from room temperature to 400 °C at a heating rate of 10 °C min⁻¹. Dispersion was calculated according to mmol g⁻¹ of H₂ adsorbed on each sample, metal content of nickel (5 wt%) and 1:1 Ni:H stoichiometry, metal content of tungsten (2.5 wt%) and 1:1 W:H stoichiometry and metal content of gold (2.5 wt%) and 1:1 Au:H stoichiometry.

3. Results and Discussion

3.1. Materials Characterization

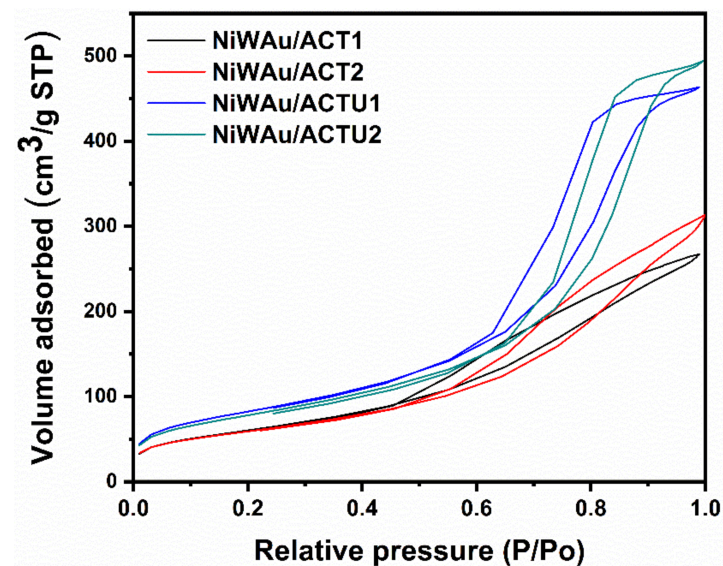
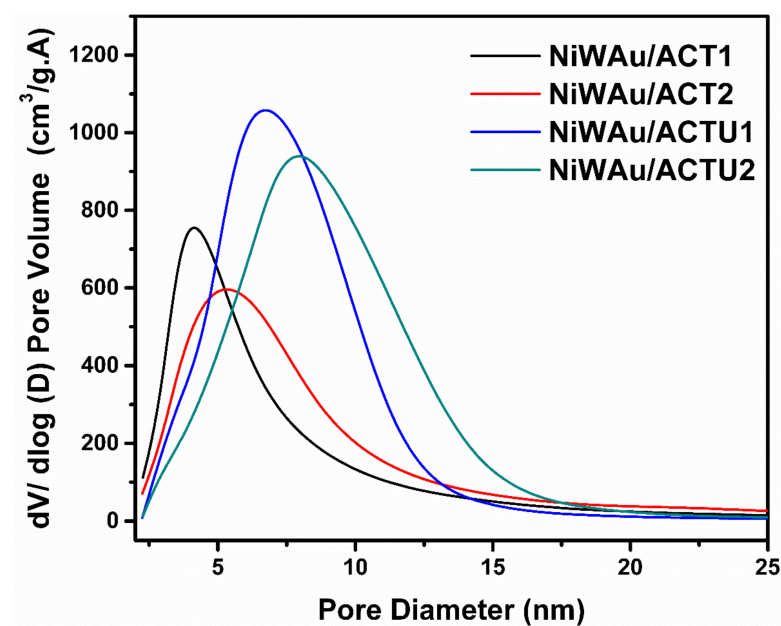
3.1.1. BET Specific Surface Area (SSA)

The nitrogen physisorption results of the supports and the supported bimetallic and trimetallic NPs catalysts are listed in Table 2. The supported NiWAu trimetallic NPs are mesoporous amorphous solids with high SSA in the range of 220 to 215 m² g⁻¹ for the catalysts impregnated by wet impregnation plus recharge method; on the other hand, for the trimetallic catalysts impregnated by ultrasound method plus recharge method, the SSA was increased in the range of 280 to 290 m² g⁻¹. Another important observation deals with the increasing SSA of the four supported NiWAu trimetallic NPs with respect to the four supported NiW bimetallic NPs, indicating that the recharge method plays an important role in the support and metal redispersion [36].

Figure 2 shows the adsorption–desorption isotherms of the prepared catalysts, showing type IV isotherms according to the IUPAC, which are characteristic of a mesoporous material ranging from 2 to 50 nm, with a hysteresis curve type H1 characteristic of the geometry of tubular shaped capillaries opened at the ends and capillaries shaped like an ink bottle. In Figure 3, it can be observed that the average pore diameters ranged from 8 to 14 nm.

Table 2. BET specific surface area (SSA) of the supports and metallic nanomaterials.

Materials	BET SSA (m ² /g)	Materials	BET SSA (m ² /g)
ACT1	382	Ni/ACTU1	263
ACT2	367	Ni/ACTU2	277
Ni/ACT1	233	NiW/ACTU1	214
Ni/ACT2	225	NiW/ACTU2	233
NiW/ACT1	218	NiWAu/ACTU1	290
NiW/ACT2	179	NiWAu/ACTU2	280
NiWAu/ACT1	220		
NiWAu/ACT2	215		

**Figure 2.** BET adsorption–desorption isotherms for the four supported trimetallic NPs nanomaterials.**Figure 3.** Pore distribution of the four supported trimetallic NPs nanomaterials synthesized by the recharge method.

3.1.2. X-ray Diffraction (XRD)

Figure 4 displays the XRD patterns of NiW/ACT1 and NiWAu/ACT1 fresh nanomaterial samples. The diffraction patterns of prepared support and bimetallic and trimetallic NPs supported on ACT1 can be seen. After the thermal treatments of reduction, it was observed that the NiW/ACT1 and NiWAu/ACT1 fresh samples preserved the crystalline phases of gamma-alumina and the anatase phase of titania. The diffraction peak at 37.65° indicates the formation of very small NiO crystallites [38,39]. Figure 4 also shows the diffraction patterns of Au in NiWAu/ACT1, where peaks at 38.30 , 44.48 , 64.82 and 77.77° correspond to the (111), (200), (220) and (311) crystalline planes of gold. Representing a face-centered cubic (FCC) structure of the gold NPs on the support surface, gold is added in a metallic form due to the reduction by hydrogen adsorbed in nickel and tungsten [8,29]. An oxide-reduction process occurs, causing metal–metal–metal interaction.

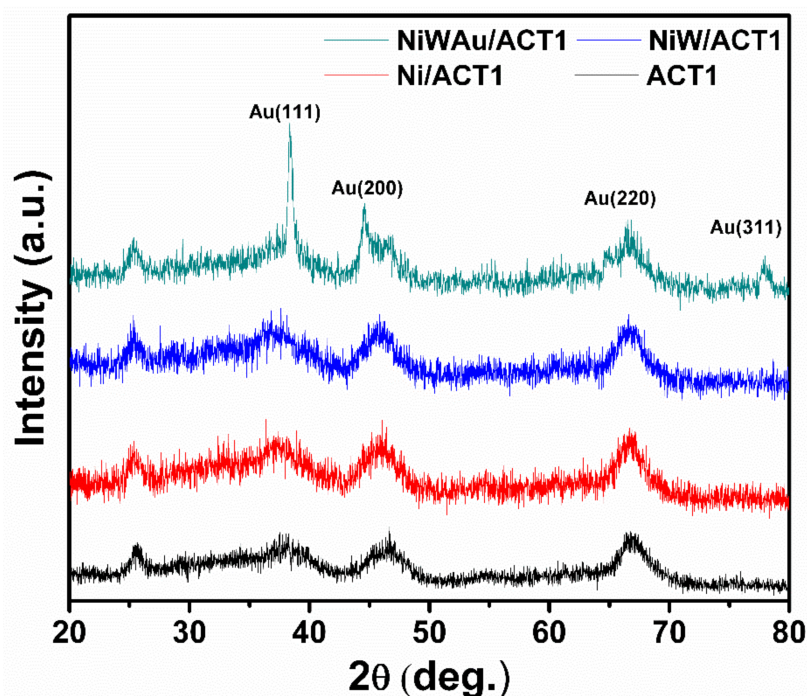


Figure 4. XRD patterns of NiWAu/ACT1 nanomaterials and support.

Figure 5 shows the X-ray diffraction patterns of the deposited gold catalysts in NiWAu/ACT1, NiWAu/ACT2, NiWAu/ACTU1 and NiWAu/ACTU2 that are used to identify crystalline phases of the nanostructured materials. For all samples, the diffraction peaks were observed for the Au nanoparticles at 38.30 , 44.48 , 64.82 and 77.77° . The average particle size of the four supported trimetallic NPs was estimated using the Scherrer equation, providing an average particle size of gold smaller than 5 nm (see Table 3). The increase in the intensity of the peaks at 46.44 and 66.75° is due to the formation of NiAl_2O_4 nickel aluminate in the four trimetallic nanomaterials; this is confirmed by UV-Vis DRS, which shows the NiAl_2O_4 formation, i.e., a spinel phase nanostructure [39].

Table 3. Au particle size from XRD and TEM data.

Materials	Average Au Particle Size by DRX (nm)	Average Au Particle Size by TEM (nm)
NiWAu/ACT1	4.2	5.4
NiWAu/ACT2	4.0	6.3
NiWAu/ACTU1	3.8	4.8
NiWAu/ACTU2	5.4	5.5

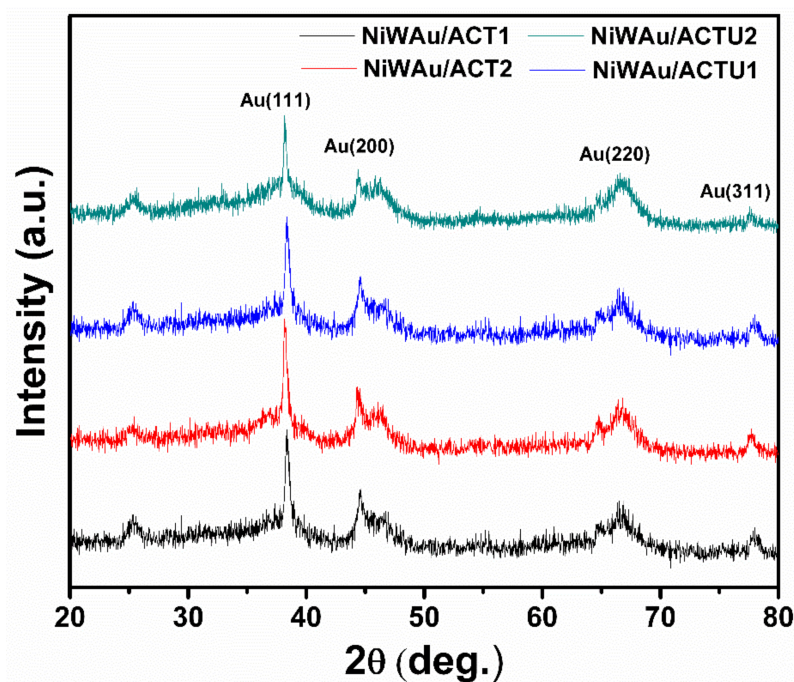


Figure 5. XRD patterns of NiWAu/ACT and NiWAu/ACTU nanomaterials.

3.1.3. UV-Vis with Diffuse Reflectance of Solids (UV-Vis DRS)

Figure 6 shows the results of UV-Vis reflectance spectroscopy for nanomaterials with gold. The TiO_2 bands are related to the charge transfer of $\text{O}^{2-} \rightarrow \text{Ti}^{4+}$; the presence of crystalline CeO_2 absorbs strongly in the UV region close to 400 nm [40]. There is the presence of absorption bands at wavelengths below 350 nm, and this indicates the existence of fine crystallites, not detectable by XRD. The bands at 526 and 634 nm are assigned to Ni^{2+} ions in the tetrahedral symmetry in the lattice of Al_2O_3 , and they are associated with the formation of the spinel phase Ni_2O_4 also detected by XRD [41]. The UV-Vis DRS studies suggest the formation of surface $\text{Ni}/\text{Al}_2\text{O}_3$ across the bands at 598 and 636 nm. The peaks at 462 and 710 nm are characteristic of NiO crystallites formation. The band at 710 nm is associated with octahedral Ni^{2+} symmetry and presents low intensity. These latter interactions of $\text{Ni}/\text{Al}_2\text{O}_3$ and the formation of NiO crystals are also seen in XRD [39,42].

Absorption bands were shown at 300 to 350 nm corresponding to W^{6+} species and Ni-W-support interactions. W^{6+} and WO_x species in tetrahedral coordination, with octahedral symmetry Ni ions, $\text{Ni}[\text{Ni}^{2+}6\text{O}^{-2}]$, and WO_x species in octahedral coordination with Ni ions $[\text{Ni}^{2+}4\text{O}^{-2}]$ with tetrahedral symmetry were also shown.

The position of the Au band in the metallic state is generally accepted as between 500 and 600 nm (plasmon band). The band position of the Au species is undefined; however, it has been reported that the Au^+ cations exhibit an absorption band at around 240 nm, while small clusters such as $(\text{Au})_n^{\delta+}$ exhibit a band at around 390 nm [43]. A band at 525 nm is shown, which is typical of the Au plasmon, because of small metallic Au particles in the trimetallic catalysts, which confirms the presence of Au^0 . The type of absorption band is due to the partial loading of gold nanoparticles. A higher peak in XRD/UV-Vis implies a larger particle size [44,45].

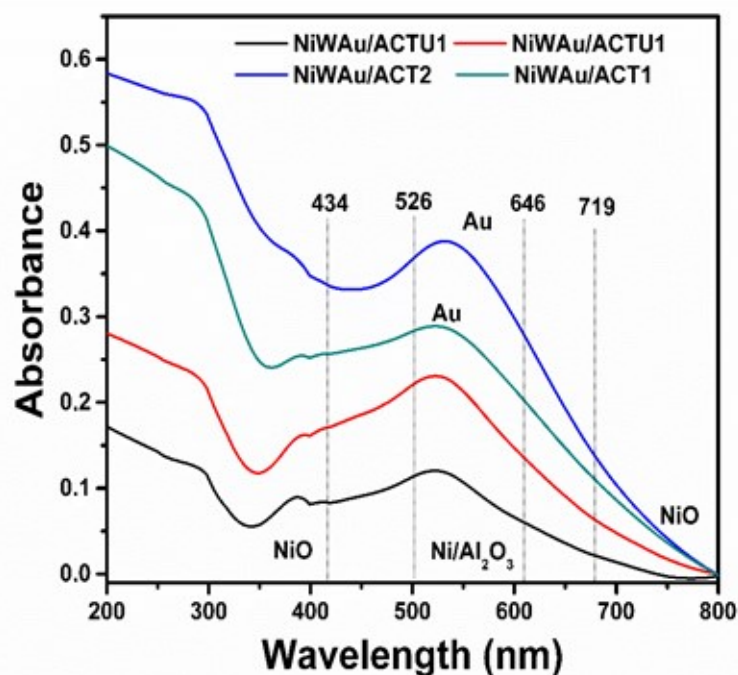


Figure 6. UV-Vis with diffuse reflectance of solids (DRS) for nanomaterials synthesized by the recharge method.

3.1.4. Scanning Electron Microscopy (SEM)

Figure 7 shows the SEM image and the energy-dispersive spectrometry (EDS) elemental mapping images of a selected region of NiWAu/ACT1. The analysis of Ni, W and Au elemental mapping suggested that the trimetallic NPs are homogeneously distributed over the entire support surface and showed heterogeneous morphology of the support ACT1 consisting of crystals of different sizes, shapes and orientations.

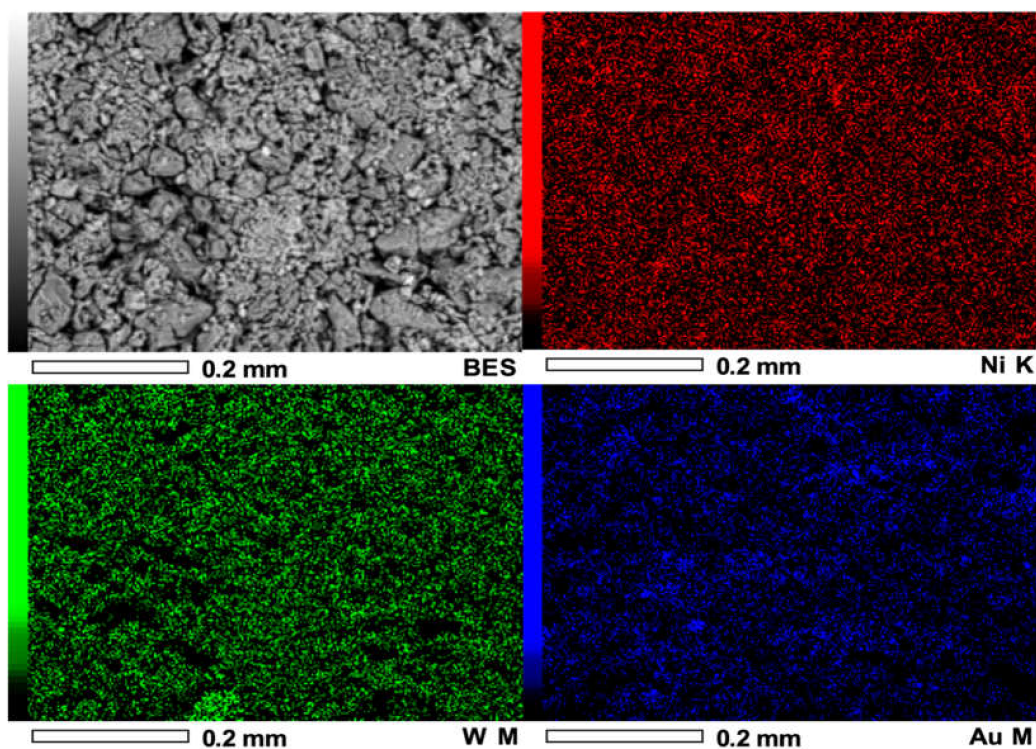


Figure 7. EDX elemental chemical mapping of NiWAu/ACT1 nanomaterial.

The elemental composition of the NiW Au trimetallic NPs supported on Al₂O₃-CeO₂-TiO₂ synthesized by two different routes is reported in Table 4. It highlights a fact concerning the final total loading of Ni and Au in the trimetallic NPs. The impregnating solutions were adjusted to reach a nominal Au loading of 2.5 wt% and Ni loading of 5 wt%. However, lower values of Au loading of 2.5 wt% and Ni loading of 5 wt% were obtained with the preparation route that was selected by ultrasound plus recharge method, which is opposite to that observed in the case of supported trimetallic NPs prepared by wet impregnation plus recharge method. Therefore, the Au loading of the NiW Au/ACT1 was very close to the target gold content, indicating the enhanced resistance against the loss of the Au precursor after the synthetic method of trimetallic NPs. This latter result shows the effect of the preparation methods, and it could be related to a stronger interaction of the support with the NiW Au trimetallic NPs. The presence of NiAl₂O₄ nickel aluminate and Ni-W-O is evidence of a close intimate interaction between metals and support that indeed promotes their redox properties.

Table 4. EDX quantitative analysis of trimetallic nanomaterials NiW Au NPs supported on Al₂O₃-CeO₂-TiO₂.

NiW Au/ACT1		NiW Au/ACTU1	
Chemical Elements	ms%	Chemical Elements	ms%
O	45.8	O	44.3
Al	36.6	Al	43.5
Ti	7.0	Ti	5.3
Ni	5.0	Ni	1.1
Ce	1.0	Ce	2.2
W	2.3	W	2.2
Au	2.3	Au	1.4
Total	100	Total	100

Figure 8 displays the mutual overlap of three EDX elemental maps, Ni, Au and W. From the EDX image, it was indicated that Au and Ni elements were intermixed, showing gold NPs predominant with a good dispersion on the Ni surface near the support lattice. It can be concluded that the nickel NPs are incorporated in the gold matrix due to the metallic interaction between nickel and gold [46–48]. Metal–support interactions in the supported catalysts have been detected when the incorporation of metals into the framework of a support lattice occurs [49,50]. In this work, the metal–metal–support interaction (Ni-W-O) and NiAl₂O₄ also could be seen in the UV-Vis DRS results for the four trimetallic supported NPs nanomaterials. In fact, the recharge method influenced the redistribution of the metals in the boundary of the support, which probably provoked a redispersion effect of the metals on the catalyst surface and the intimate contact between metals and support. The morphological micrograph observed in Figure 9 is for Au/NiW/Al₂O₃-CeO₂-TiO₂ synthesized by the recharge method. By correlating data from DRX and UV-Vis DRS, Figure 10 shows the deposit of the nanometer gold around the NiO crystallites.

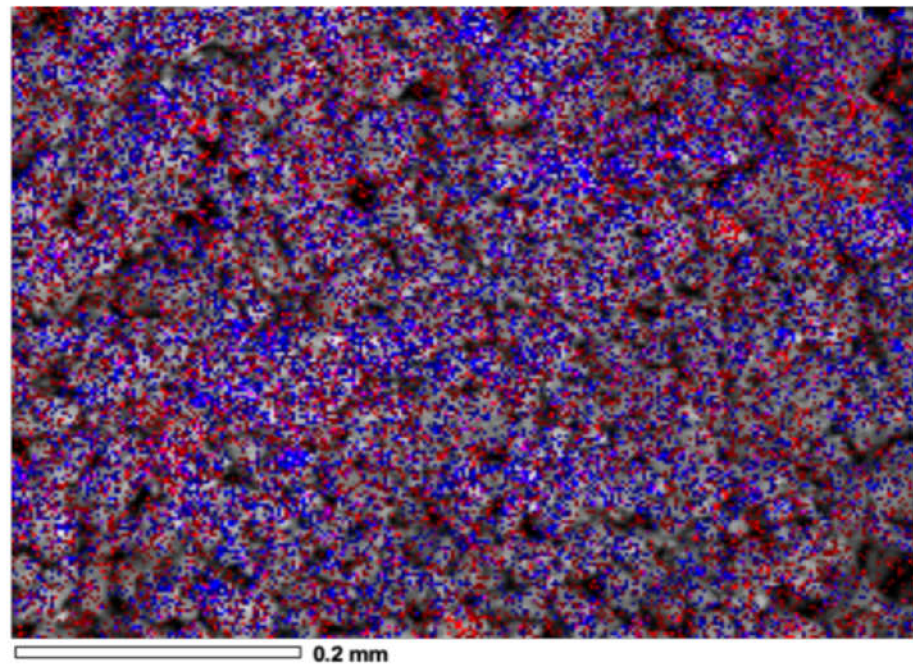


Figure 8. Overlapping EDX elemental mapping of NiWAu/ACT1 nanomaterial with gold at 2.5 wt%.

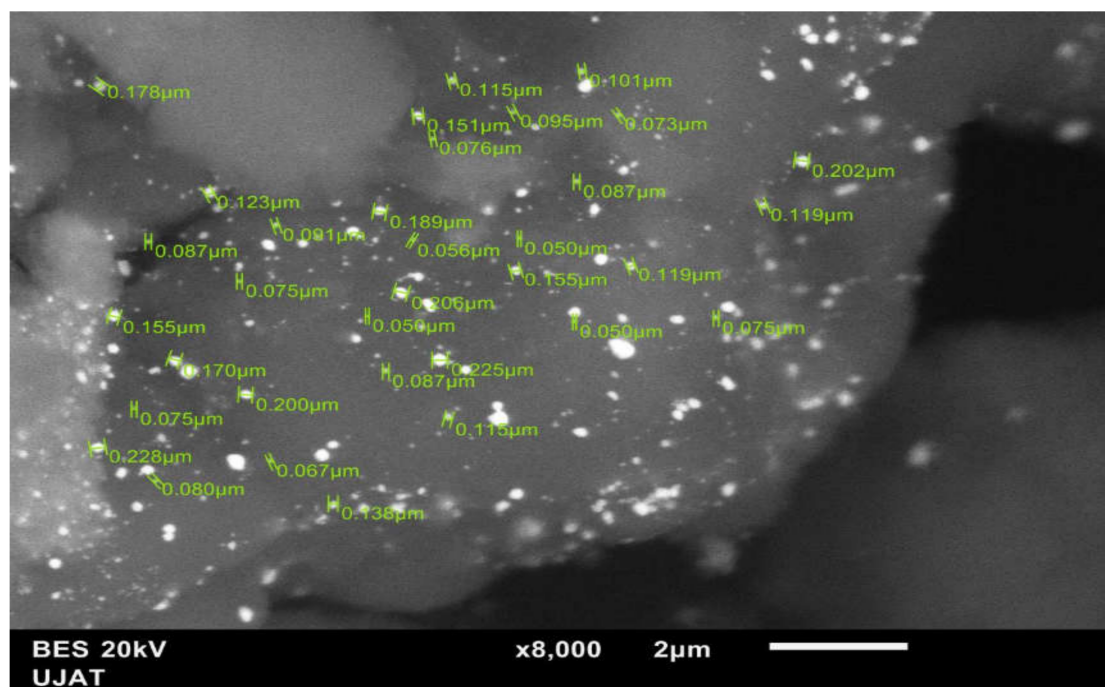


Figure 9. SEM images with BES detector for the nanomaterial NiWAu/ACT1.

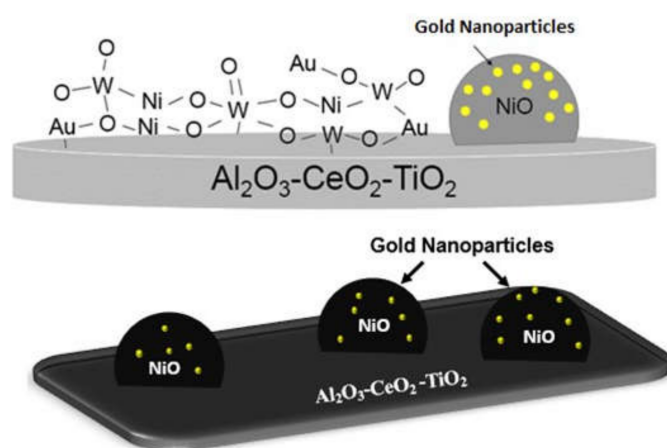


Figure 10. Nanoparticles of Ni and Au distributed on the support for NiWAu/ACT1 nanomaterial.

3.1.5. Transmission Electron Microscopy (TEM)

Representative TEM images and particle size distributions of fresh supported trimetallic NPs NiWAu/ACT1, NiWAu/ACTU1, NiWAu/ACT2 and NiWAu/ACTU2 can be appreciated in Figure 11. For each sample, about 200 individual particles randomly selected in a unique zone of the nanomaterial were analyzed. The metal nanoparticles of gold, nickel and tungsten appeared darker in the images because they showed strong electron diffraction. In the two samples, the shape of the particles mostly is spherical or quasispherical, although a few particles represented cylindrical shape. The TEM image of supported NiWAu trimetallic NPs showed several agglomerates and many separated or isolated spherical trimetallic NPs distributed over the whole surface [44,48]. Analysis of the particle size distributions shows a medium distribution with most of the particle sizes ranging between 1 and 12 nm. The average particle size of the trimetallic NPs were 5.4, 6.3, 4.8 and 5.5 nm for NiWAu/ACT1, NiWAu/ACT2, NiWAu/ACTU1 and NiWAu/ACTU2, respectively. Similar values of the particle size were obtained from the XRD line width (see Table 3).

3.1.6. Temperature-Programmed Desorption of Hydrogen (TPD-H₂)

The accessibility of nickel, tungsten and gold was determined from the thermogram areas of the TPD-H₂, assuming a stoichiometry of H/Ni=1, H/W=1 and H/Au=1 taking into account the values of Table 5 for calculations.

Table 5. Metal surfaces (S_G) and densities of metals.

Metal	S_G (m ² /g)	ρ (g/cm ³)
Ni	654	8.90
W	753	19.35
Au	266	19.32

These thermograms of TPD-H₂ show the peaks originating from the desorption of hydrogen. The area under the curve of Figure 12 represents the desorbed moles of hydrogen in the material, and therefore, each peak represents a desorption temperature. Additionally, the TPD-H₂ method was used to define the types of catalytic active sites for hydrogen chemisorption and activation; furthermore, it was used to determine the influence that gold addition might have on the nature of catalytic active sites.

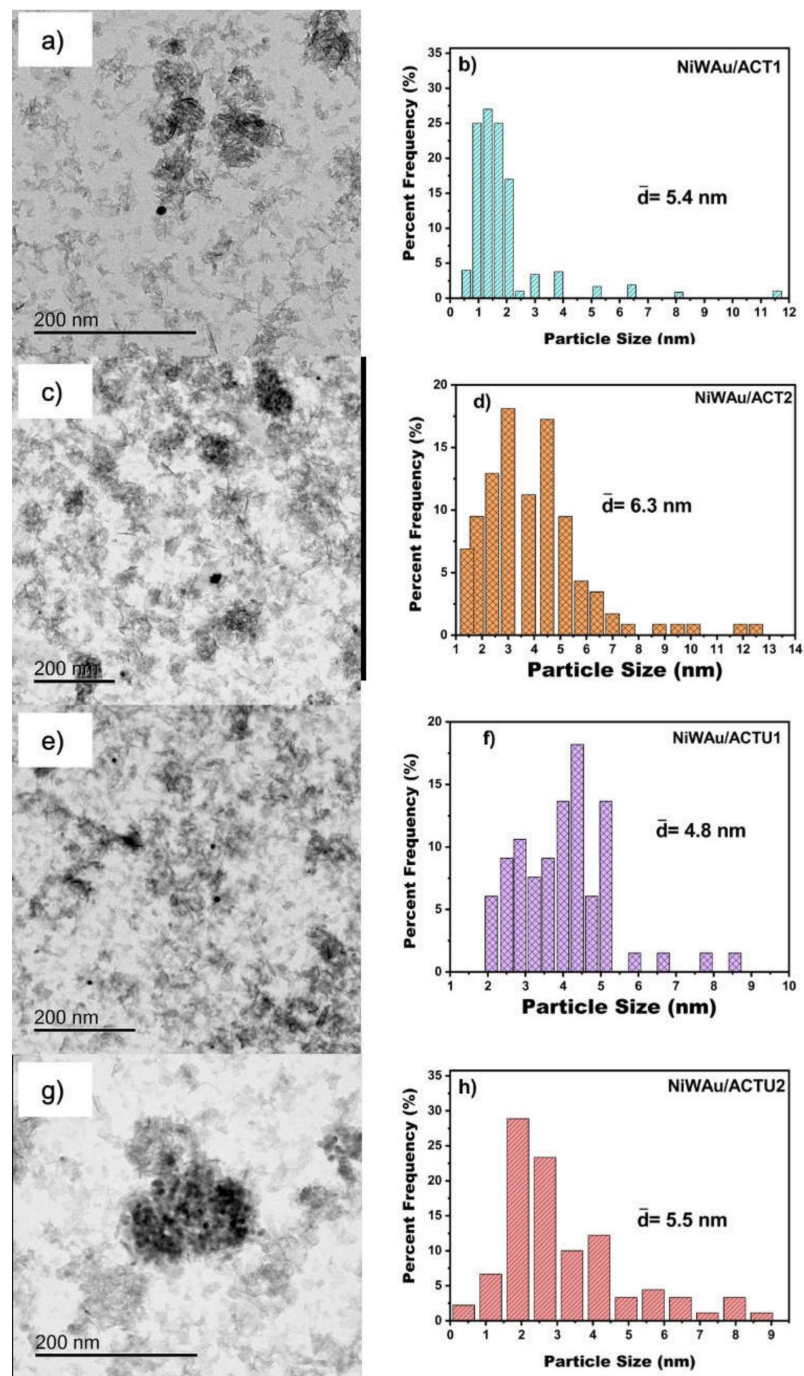


Figure 11. TEM image and particle size distributions (right side) of the nanomaterials (a,b) NiWAu/ACT1, (c,d) NiWAu/ACT2, (e,f) NiWAu/ACTU1 and (g,h) NiWAu/ACTU2 prepared by the recharge method.

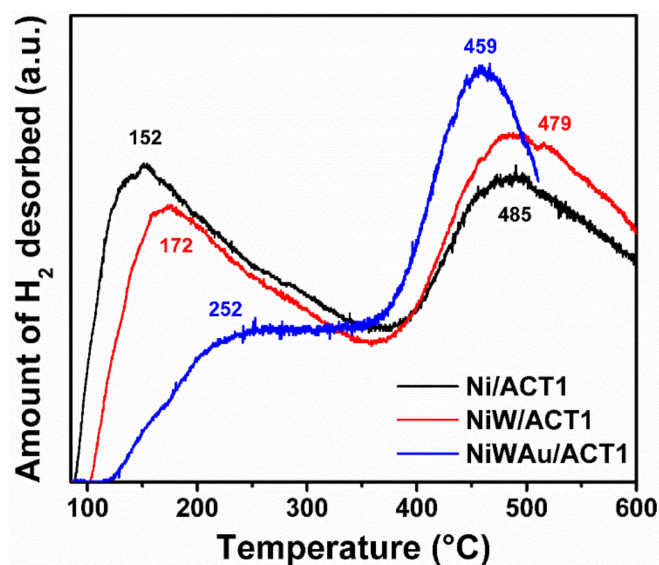


Figure 12. TPD-H₂ profiles of reduced trimetallic nanomaterials at 400 °C.

Figure 12 shows the TPD-H₂ profiles of supported NiW bimetallic NPs prepared by two different sequential methods (ultrasound and wet impregnation) and Au/NiW trimetallic NPs prepared after gold addition over the supported NiW bimetallic NPs. All the nanomaterials studied had two characteristic peaks in their TCD signal profile. Furthermore, the TPD-H₂ profiles have two domains of H₂ desorption peaks. The first domain includes desorption peaks at lower temperatures, at around 150–250 °C. The second domain is situated at higher temperatures, at around 450–490 °C. The first domain is largely recognized to represent hydrogen desorbed from metallic nanoparticles. The second one can be ascribed to hydrogen originally located on subsurface layers and/or to spillover hydrogen [51,52]. The H₂ spillover occurs during the prereluction step of TPD-H₂ experiments, when the hydrogen atoms are dissociated over the nanometallic surface and migrate to subsurface layers and/or to the support, generating hydrogen species strongly bonded to the nanomaterial surface. The peaks related to exposed trimetallic NPs and active metal sites are located at lower temperatures [21,51].

The metal accessibility and the particle size present in the supported NiW bimetallic and AuNiW trimetallic NPs were determined using the values of the Table 5 (metal surface and densities) and the results obtained by TPD-H₂ profiles shown in Table 6. It was observed that when gold was added to the NiW bimetallic nanomaterials synthesized by the impregnation method, the dispersion of metallic surface species improved significantly, therefore increasing the exposed trimetallic surface %D.

The results of nitrogen physisorption showed values of high specific areas that increased after the addition of Au by the recharge method due to the redispersion of the metals and the support in the catalyst, allowing the migration of Ni and W atoms. Moreover, there was an increase in metal dispersion or accessibility (%D) obtained by TPD-H₂ where the available metallic surfaces increased when gold was added due to the effect of the recharge method, resulting in metallic crystallite average size values of around 1.7 to 2.1 nm, which correspond to well-dispersed gold, nickel and tungsten nanoparticles in the synthesized trimetallic nanomaterials.

One advantage of the wet impregnation method is that there is no loss of material on the first and second metals (Ni and W) deposited over the support; this causes a synergy to deposit the proposed theoretical Au content. On the contrary, for the ultrasound method, there was a loss of more than one-half of nickel and one-half of gold impregnated. Furthermore, the deposit of the nanometric gold is limited by the amount of the first two metals in the support. The average trimetallic (gold, nickel and tungsten) particle size measured though TPD-H₂ was smaller when impregnation and recharge methods were selected for preparation.

Table 6. Total dispersion (%) and metal crystallite sizes of the NiWAu/ACT nanomaterials by TPD-H₂.

Sample	BET Area (m ² /g)	Average Au Particle Size (nm) ^a	HTC ((μmol H ₂ /gcat)	TPD-H ₂ (H/M = 1 μmol H ₂ /gcat)	% D (H/M)	MCS (nm) ^b
NiW/ACT1	214	-	0.85	0.60	70	1.5
NiW/ACT2	179	-	0.85	0.63	74	1.4
NiW/ACTU1	218	-	2.47	0.65	26	3.3
NiW/ACTU2	179	-	2.47	0.55	22	3.9
NiWAu/ACT1	220	4.2	0.99	0.46	46	1.8
NiWAu/ACT2	215	4.0	0.99	0.50	50	1.7
NiWAu/ACTU1	290	3.8	0.99	0.33	33	2.6
NiWAu/ACTU2	280	5.4	0.99	0.41	41	2.1

^a Calculated from XRD data, with Scherrer's equation. ^b MCS (nm) calculated from TPD-H₂ data. MCS = average metal crystallite size. % D = percentage of metallic dispersion.

3.1.7. Structural and Catalytic Properties of Nanomaterials

The trimetallic supported nanocatalysts developed and synthesized in this study possess particular structural properties allowing them to be used for several catalytic applications. The close intimate interaction between metals and support (strong metal–support interaction) is a highly desirable structural property for nanocatalysts as it promotes their redox properties [53,54]. The strong metal–support interaction has a relationship with the number of oxygen vacancies in the support [54–56]. CeO₂ has attracted much interest in the oxidation process due to its high oxygen storage capacity and unique redox ability. Its ability to store and release oxygen due to the effective redox Ce⁴⁺/Ce³⁺ sites that enable the exchange of oxygen via oxygen vacancy significantly increases the performance of catalytic systems and suppresses the deactivation of catalysts under rigorous reaction conditions [57,58]. For the degradation of refractory organic compounds (ROCs), it has been reported that the oxygen storage capacity (OSC) and the redox properties of ceria should be increased by the introduction of other transition and nontransition metal ions; therefore, many ceria-based catalysts have been developed, such as CeO₂-ZrO₂ [57–61], CeO₂-TiO₂ [62–64], CeO₂-WO₃ [65], CeO₂/Al₂O₃ [66,67] and CeO₂-SiO₂ [68–70]. Besides, the species Ti³⁺ for the TiO₂ support is related to oxygen vacancies as a result of lattice distortion or surface defects [71].

This oxygen vacancy is beneficial for forming reactive centers or yielding active oxygen, especially beneficial for oxidation degradation. They are acid sites called Lewis sites where a nucleophilic substrate can be deposited [72]. Previous works have proved that the number of acid sites promotes efficient catalytic properties (e.g., in catalytic wet air oxidation of ROCs [37,54,73–76] and production of biofuels [77–79]).

The catalytic activity of degradation of ROCs via CWAO using heterogeneous nanocatalysts has been improved to increase the OSC directly associated with oxygen vacancies. The oxidation mechanism proposed by our group shows that such vacancies are directly involved in the oxygen activation reaction at the catalyst surface and, consequently, the creation of highly reactive surface oxygen species such as superoxides and peroxides [54,80–83]. The oxidation of ROCs can start by activating the oxygen molecule or the ROC, and oxygen may participate in the reaction as an adsorbed species on the catalyst surface. The Lewis acid sites could activate the electronic doublet of oxygen [53,73,74]. In any case, the presence of a nanocatalyst creates an ionic environment that favors the heterolytic reactions. In the case of aromatic compounds such as phenol, the ring-opening reaction can be produced either by a free redox radical mechanism (hemolytic rupture) or by an ionic (heterolytic) mechanism [73].

The mineralization process can be explained by the transformation of the aromatic compounds into aliphatic compounds by the ring-opening reactions. The aromatic molecule ring is oxidized to catechol, hydroquinone and benzoquinones (intermediates). Successively, the ring breaks into carboxylic organic acids of low molecular weight (<C6) such as carboxylic acids (maleic acid, acetic acid, formic acid, oxalic acid). In other words, the catalytic oxidation degradation pathway of phenol includes the hydroxylation (hydroquinone, catechol, o-benzoquinone) and organic acids until preferably producing CO₂ and H₂O [84–86]. When the mechanism includes the formation of oxidized C₆-aromatic of hydroquinone and catechol, the occurrence of both compounds indicates parallel reaction pathways [87]. The presence of catechol and hydroquinone may be attributed to hydroxyl radical attack at ortho and para positions of the aromatic ring due to the resonance effect of phenol. Apart from the above reactions, a solid residue may be also formed as a result of the combination of phenyl radical with hydroquinone and p-benzoquinone through a series of chain reactions [88]. Acetic acid is especially accumulated in the system, which could be considered as the final product. If the mineralization process reaches complete total oxidation, the conversion of organic molecules to CO₂ and H₂O occurs. The TOC yield removal will be 100% of CO₂. Therefore, the TOC removal parameter is directly associated with the selectivity of CO₂. However, partial oxidation commonly occurs, and this causes the simultaneous presence of intermediates and CO₂ in the reaction mixture. Nevertheless, the increase in TOC removal means that the organic refractory molecule will be more oxidized to CO₂ [74–76].

It was found by our group that CeO₂, due to its ability to store and release oxygen and the effective redox Ce⁴⁺/Ce³⁺ occurring in its oxygen vacancies, plays an important role in enhancing the CO₂ selectivity as explained by several authors. The formation of Ce⁴⁺-O₂⁻-M at the interface could favor oxygen transfer between the nanocatalyst surface and the adsorbed species by a redox mechanism. It is important to highlight with our findings that the excess of Ce loading (50 wt%) increases OSC, which favors the para-oxidation of phenol and the consequent occurrence of carbon deposit by the polymer formation from p-benzoquinone and the decrease in the number of Lewis sites. It was established by our group that the number of total sites increases for the monometallic (Ru/ZrO₂-CeO₂) and bimetallic (RuAu/ZrO₂-CeO₂) catalysts by Ce loading of 10 wt%, and this enhances the ortho-oxidation of phenol. On the contrary, the number of total sites decreases when the Ce loading reaches 20 wt% in RuAu/ZrO₂-CeO₂ catalysts [53]. Another important contribution by our group is the finding that if the route takes place by the formation of the quinones, the polymerization on the surface of the catalysts is important; therefore, the deactivation of the material can be carried out due to the blocking of the superficial active sites [74,88].

Furthermore, another important application that has been discussed by our group is the production of biofuels through biomass. The conversion of glucose to produce 5-hydroxymethylfurfural (HMF) using TiO₂-ZrO₂ binary oxides and Al₂O₃-TiO₂-W has been researched. The number of acid sites plays an important role in achieving the highest 5-HMF yield [76–79].

4. Conclusions

Four NiWAu supported trimetallic NPS nanomaterials were prepared by a three-step synthetic method in which the gold addition was the last step via the recharge method. The effect of the gold addition using the recharge method on the structural and chemical properties of NiW/Al₂O₃-CeO₂-TiO₂ was investigated. The TPD-H₂ results obtained revealed that the addition of gold synthesized by impregnation plus recharge method improved the dispersion of trimetallic surface species (46% and 50%). The particle size of gold from XRD and TEM data in NiWAu/ACTU1 was smaller using impregnation plus ultrasound recharge method than impregnation plus recharge in NiWAu/ACT1.

The recharge method promoted nanostructures of gold nanoparticles <6.5 nm in the four NiWAu trimetallic catalysts supported on mixed oxides. After the addition of gold in

the four supported bimetallic NiW systems, the specific surface areas (SSAs) were larger than those of the bimetallic systems. This method provided the rearrangement of the metallic surface, which provoked a redispersion effect of the metals on the catalyst surface. Gold is added in its metallic form due to the reduction produced by the adsorbed hydrogen in the supported Ni-W bimetallic NPs surfaces.

The gold addition for the supported NiW/ACT1, NiW/ACT2, NiW/ACTU1 and NiW/ACTU2 bimetallic NPs enhanced the formation of NiAl₂O₄ nickel aluminate, Ni-W-O and Ni-Au-O phases, which were shown to be strong metal-support interaction species that have close intimate interaction between metals and support. These changes could not be seen in the four bimetallic systems.

Author Contributions: Conceptualization, methodology, validation, formal analysis, investigation, writing—original draft, data curation, J.C.-E.; writing—original draft, writing—review and editing, software, supervision, visualization, Z.G.-Q.; writing—original draft, writing—review and editing, software, supervision, visualization, I.C.-L.; writing—original draft, writing—review and editing, software, supervision, visualization, A.E.E.d.l.M.; writing—original draft, writing—review and editing, software, supervision, visualization, M.A.L.-R.; writing—original draft, writing—review and editing, software, supervision, visualization, J.C.A.-P.; writing—original draft, writing—review and editing, software, supervision, visualization, A.A.S.-P.; writing—original draft, writing—review and editing, software, supervision, visualization, A.C.-G.; writing—original draft, writing—review and editing, software, supervision, visualization, A.C.-U.; conceptualization, methodology, project administration, funding acquisition, writing—original draft, J.G.T.-T. All authors have read and agreed to the published version of the manuscript.

Funding: This research was funded by the National Council of Science and Technology Project No. 132648 Cátedras-CONACYT Program Project Number 1024 and the PFCE-UJAT-DACB 2019–2020.

Institutional Review Board Statement: Not applicable.

Informed Consent Statement: Not applicable.

Data Availability Statement: Data are contained within the article.

Acknowledgments: This research was supported by the National Council of Science and Technology (CONACYT) by the scholarship granted to Postgraduate Studies of Science with Material Orientation to Jorge Cortez Elizalde, within the graduate program of the Universidad Juárez Autónoma de Tabasco. The authors are thankful for support from the CONACYT Project No. 132648, Cátedras-CONACYT Program Project Number 1024, the Universidad Juárez Autónoma de Tabasco and the Education Ministry Public of Mexico through the PFCE-UJAT-DACB 2019–2020 program.

Conflicts of Interest: The authors declare no conflict of interest.

References

1. Jia, C.J.; Schüth, F. Colloidal metal nanoparticles as a component of designed catalyst. *Phys. Chem. Chem. Phys.* **2011**, *13*, 2457–2487. [[CrossRef](#)]
2. Khalil, M.; Jan, B.M.; Tong, C.W.; Berawi, M.A. Advanced nanomaterials in oil and gas industry: Design, application and challenges. *Appl. Energy* **2017**, *191*, 287–310. [[CrossRef](#)]
3. Mazzieri, V.A.; Grau, J.M.; Vera, C.R.; Yori, J.C.; Parera, J.M.; Pieck, C.L. Pt-Re-Sn/Al₂O₃ trimetallic catalysts for naphtha reforming processes without presulfiding step. *Appl. Catal. A Gen.* **2005**, *296*, 216–221. [[CrossRef](#)]
4. Dong, X.; Zheng, P.; Zheng, A.-G.; Li, H.-F.; Xia, G.-F.; Li, M.-F.; Zheng, R.-Y.; Xu, B.-Q. Noble-metal efficient Pt-Ir-Co/SiO₂ catalyst for selective hydrogenolytic ring opening of methylcyclopentane. *Catal. Today* **2018**, *316*, 162–170. [[CrossRef](#)]
5. Zhang, H.; Pei, A.; Liao, J.; Ruan, L.; Yang, K.; Wang, J.; Zhu, L.; Chen, B.H. PtRuNi/C novel nanostructures of platinum-ruthenium island-on-Ni/Ni(OH)₂ nanoparticles for the selective hydrogenation of quinoline. *J. Alloys Compd.* **2020**, *834*, 155203. [[CrossRef](#)]
6. Yurderi, M.; Bulut, A.; Zahmakiran, M.; Kaya, M. Carbon supported trimetallic PdNiAg nanoparticles as highly active, selective and reusable catalyst in the formic acid decomposition. *Appl. Catal. B Environ.* **2014**, *160–161*, 514–524. [[CrossRef](#)]
7. Cunha, E.M.; Ribeiro, J.; Kokoh, K.B.; De Andrade, A.R. Preparation, characterization and application of Pt-Ru-Sn/C trimetallic electrocatalysts for ethanol oxidation in direct fuel cell. *Int. J. Hydrogen Energy* **2011**, *36*, 11034–11042. [[CrossRef](#)]
8. Jawad, M.; Ali, S.; Waseem, A.; Rabbani, F.; Amin, B.A.Z.; Bilal, M.; Shaikh, A.J. Plasmonic effects and size relation of gold-platinum alloy nanoparticles. *Adv. Nano Res.* **2019**, *7*, 167–180.

9. Yang, L.; Su, J.; Luo, W.; Cheng, G. Strategic synthesis of graphene supported trimetallic Ag-based core-shell nanoparticles toward hydrolytic dehydrogenation of amine boranes. *Int. J. Hydrogen Energy* **2014**, *39*, 3360–3370. [[CrossRef](#)]
10. Jin, F.; Fu, Y.; Kong, W.; Wang, J.; Cai, F.; Zhang, J.; Xu, J. Dry reforming of methane over trimetallic NiFeCu alloy catalysts. *Chem. Phys. Lett.* **2020**, *750*, 137491. [[CrossRef](#)]
11. Karatas, Y.; Bulut, A.; Yurderi, M.; Ertas, I.E.; Alal, O.; Gulcan, M.; Celebi, M.; Kivrak, H.; Kaya, M.; Zahmarikan, M. PdAu-MnOx nanoparticles supported on amine-functionalized SiO₂ for the room temperature dehydrogenation of formic acid in the absence of additives. *Appl. Catal. B Environ.* **2016**, *180*, 586–595. [[CrossRef](#)]
12. Lua, A.C.; Wang, H.Y. Hydrogen production by catalytic decomposition of methane over Ni-Cu-Co alloy particles. *Appl. Catal. B Environ.* **2014**, *156–157*, 84–93. [[CrossRef](#)]
13. Tsoncheva, T.; Ivanova, R.; Henych, J.; Dimitrov, M.; Kormunda, M.; Kovacheva, D.; Scotti, N.; Santo, V.D.; Štengl, V. Effect of preparation procedure on the formation of nanostructured ceria–zirconia mixed oxide catalysts for ethyl acetate oxidation: Homogeneous precipitation with urea vs. template-assisted hydrothermal synthesis. *Appl. Catal. A Gen.* **2015**, *502*, 418–432. [[CrossRef](#)]
14. Roy, B.; Martinez, U.; Loganathan, K.; Datye, A.; Leclerc, C. Effect of preparation methods on the performance of Ni/Al₂O₃ catalysts for aqueous-phase reforming of ethanol: Part I-catalytic activity. *Int. J. Hydrogen Energy* **2012**, *37*, 8143–8153. [[CrossRef](#)]
15. Benito, P.; Gregori, M.; Andreoli, S.; Fornasari, G.; Millefanti, S.; Ospitali, F.; Albonetti, S. Role of the preparation method on properties of Pd/Cu-MCM-41 hydrodechlorinating catalysts. *Catal. Today* **2014**, *235*, 134–143. [[CrossRef](#)]
16. Manzoli, M.; Menegazzo, F.; Signoreto, M.; Cruciani, G.; Pinna, F. Effects of synthetic parameters on the catalytic performance of Au/CeO₂ for furfural oxidative esterification. *J. Catal.* **2015**, *330*, 465–473. [[CrossRef](#)]
17. Ramakrishnan, S.; Balamurugan, J.; Vinothkannan, M.; Kim, A.R.; Sengodan, S.; Yoo, D.J. Nitrogen-doped graphene encapsulated FeCoMoS nanoparticles as advanced trifunctional catalyst for water splitting devices and zinc-air batteries. *Appl. Catal. B Environ.* **2020**, *279*, 119381. [[CrossRef](#)]
18. Mendoza-Nieto, J.A.; Robles-Méndez, F.; Klimova, T.E. Support effect on the catalytic performance of trimetallic NiMoW catalysts prepared with citric acid in HDS of dibenzothiophenes. *Catal. Today* **2015**, *250*, 47–59. [[CrossRef](#)]
19. Jahel, A.; Avenier, P.; Lacombe, S.; Olivier-Fourcade, J.; Jumas, J.C. Effect of indium in trimetallic Pt/Al₂O₃SnIn-Cl naphtha-reforming catalysts. *J. Catal.* **2010**, *272*, 275–286. [[CrossRef](#)]
20. Bocanegra, S.A.; Castro, A.A.; Scelza, O.A.; de Miguel, S.R. Characterization and catalytic behavior in the n-butane dehydrogenation of trimetallic InPtSn/MgAl₂O₄ catalysts. *Appl. Catal. A Gen.* **2007**, *333*, 49–56. [[CrossRef](#)]
21. Samoilam, P.; Boutzeloit, M.; Benitez, V.; D'Ipollito, S.A.; Especel, C.; Epron, F.; Vera, C.R.; Marécot, P.; Pieck, C.L. Influence of the pretreatment method on the properties of trimetallic Pt-Ir-Ge/Al₂O₃ prepared by catalytic reduction. *Appl. Catal. A Gen.* **2007**, *332*, 37–45. [[CrossRef](#)]
22. Liang, Z.; Xiao, X.; Yu, X.; Huang, X.; Jiang, Y.; Fan, X.; Chen, L. Non-noble trimetallic Cu-Ni-Co nanoparticles supported on metal-organic frameworks as highly efficient catalysts for hydrolysis of ammonia borane. *J. Alloys Compd.* **2018**, *741*, 501–508. [[CrossRef](#)]
23. Ruth, K.; Hayes, M.; Burch, R.; Tsubota, S.; Haruta, M. The effects of SO₂ on the oxidation of CO and propane on supported Pt and Au catalysts. *Appl. Catal. B Environ.* **2000**, *24*, L133–L138. [[CrossRef](#)]
24. Tsubota, S.; Cunningham, D.; Bando, Y.; Haruta, M. Preparation of nanometer gold strongly interacted with TiO₂ and the structure sensitivity in low-temperature oxidation of CO. *Adv. Pharmacol.* **1995**, 227–235. [[CrossRef](#)]
25. Haruta, M. Novel catalysis of gold deposited on metal oxides. *Catal. Surv. Jpn.* **1997**, *1*, 61–73. [[CrossRef](#)]
26. Haruta, M. Size- and support-dependency in the catalysis of gold. *Catal. Today* **1997**, *36*, 153–166. [[CrossRef](#)]
27. Huang, Y.-F.; Huang, K.-M.; Chang, H.-T. Synthesis and characterization of Au core–Au–Ag shell nanoparticles from gold seeds: Impacts of glycine concentration and pH. *J. Colloid Interface Sci.* **2006**, *301*, 145–154. [[CrossRef](#)] [[PubMed](#)]
28. Bogireddy, N.K.R.; Martinez Gomez, L.; Osorio-Roman, I.; Agarwal, V. Synthesis of gold nanoparticles using *Coffea arabica* fruit extract. *Adv. Nano Res.* **2017**, *5*, 253–260.
29. Fonseca, J.D.S.L.; Ferreira, H.S.; Bion, N.; Pirault-Roy, L.; Rangel, M.D.C.; Duprez, D.; Epron, F. Cooperative effect between copper and gold on ceria for CO-PROX reaction. *Catal. Today* **2012**, *180*, 34–41. [[CrossRef](#)]
30. Aboukaïs, A.; Skaf, M.; Hany, S.; Cousin, R.; Aouad, S.; Labaki, M.; Abi-Aad, E. A comparative study of Cu, Ag and Au doped CeO₂ in the total oxidation of volatile organic compounds (VOCs). *Mater. Chem. Phys.* **2016**, *177*, 570–576. [[CrossRef](#)]
31. Redina, E.; Kirichenko, O.; Greish, A.; Kucherov, A.; Tkachenko, O.; Kapustin, G.; Mishin, I.; Kustov, L. Preparation of bimetallic gold catalysts by redox reaction on oxide-supported metals for green chemistry applications. *Catal. Today* **2015**, *246*, 216–231. [[CrossRef](#)]
32. Kirichenko, O.; Redina, E.; Davshan, N.; Mishin, I.; Kapustin, G.; Brueva, T.; Kustov, L.; Li, W.; Kim, C. Preparation of alumina-supported gold-ruthenium bimetallic catalysts by redox reactions and their activity in preferential CO oxidation. *Appl. Catal. B Environ.* **2013**, *134–135*, 123–129. [[CrossRef](#)]
33. Zanella, R.; Delannoy, L.; Louis, C. Mechanism of deposition of gold precursors onto TiO₂ during the preparation by cation adsorption and deposition–precipitation with NaOH and urea. *Appl. Catal. A Gen.* **2005**, *291*, 62–72. [[CrossRef](#)]
34. Besson, M.; Kallel, A.; Gallezot, P.; Zanella, R.; Louis, C. Gold catalysts supported on titanium oxide for catalytic wet air oxidation of succinic acid. *Catal. Commun.* **2003**, *4*, 471–476. [[CrossRef](#)]

35. Acosta, B.; Smolentseva, E.; Beloshapkin, S.; Rangel, R.; Estrada, M.; Fuentes, S.; Simakov, A. Gold supported on ceria nanoparticles and nanotubes. *Appl. Catal. A Gen.* **2012**, *449*, 96–104. [[CrossRef](#)]
36. Silahua-Pavón, A.A.; Torres-Torres, G.; Arévalo-Pérez, J.C.; Cervantes-Urbe, A.; Guerra-Que, Z.; Cordero-García, A.; Monteros, A.E.D.L.; Beltramini, J.N. Effect of gold addition by the recharge method on silver supported catalysts in the catalytic wet air oxidation (CWAO) of phenol. *RSC Adv.* **2019**, *9*, 11123–11134. [[CrossRef](#)]
37. Lafaye, G.; Micheaud-Especel, C.; Montassier, C.; Marecot, P. Characterization of bimetallic rhodium-germanium catalysts prepared by surface redox reaction. *Appl. Catal. A Gen.* **2002**, *230*, 19–30. [[CrossRef](#)]
38. Papageridis, K.N.; Siakavelas, G.; Charisiou, N.D.; Avraam, D.G.; Tzounis, L.; Kousi, K.; Goula, M.A. Comparative study of Ni, Co, Cu supported on γ -alumina catalysts for hydrogen production via the glycerol steam reforming reaction. *Fuel Process. Technol.* **2016**, *152*, 156–175. [[CrossRef](#)]
39. Sepehri, S.; Rezaei, M.; Garbarino, G.; Busca, G. Facile synthesis of a mesoporous alumina and its application as a support of Ni-based autothermal reforming catalysts. *Int. J. Hydrogen Energy* **2016**, *41*, 3456–3464. [[CrossRef](#)]
40. Rao, K.N.; Bharali, P.; Thrimurthulu, G.; Reddy, B.M. Supported copper-ceria catalysts for low temperature CO oxidation. *Catal. Commun.* **2010**, *11*, 863–866. [[CrossRef](#)]
41. Heracleous, E.; Lee, A.; Wilson, K.; Lemonidou, A. Investigation of Ni-based alumina-supported catalysts for the oxidative dehydrogenation of ethane to ethylene: Structural characterization and reactivity studies. *J. Catal.* **2005**, *231*, 159–171. [[CrossRef](#)]
42. Prielcel, P.; Kubička, D.; Čapek, L.; Bastl, Z.; Ryšánek, P. The role of Ni species in the deoxygenation of rapeseed oil over NiMo-alumina catalysts. *Appl. Catal. A Gen.* **2011**, *397*, 127–137. [[CrossRef](#)]
43. Kaminski, P.; Ziolk, M. Mobility of gold, copper and cerium species in Au, Cu/Ce, Zr-oxides and its impact on total oxidation of methanol. *Appl. Catal. B Environ.* **2016**, *187*, 328–341. [[CrossRef](#)]
44. Bai, M.; Xin, H.; Guo, Z.; Guo, D.; Wang, Y.; Zhao, P.; Li, J. α -Alkylation of ketones with primary alcohols driven by visible light and bimetallic gold and palladium nanoparticles supported on transition metal oxide. *Appl. Surf. Sci.* **2017**, *391*, 617–626. [[CrossRef](#)]
45. Gaweł, B.; Lambrechts, K.; Øye, G. Preparation and characterization of Au/CeO₂-Al₂O₃ monoliths. *Mater. Sci. Eng. B* **2012**, *177*, 575–580. [[CrossRef](#)]
46. Petrović, S.; Milovanović, D.; Salatić, B.; Peruško, D.; Kovač, J.; Dražić, G.; Mitrić, M.; Trtica, M.; Jelenković, B. Composition and structure of NiAu nanoparticles formed by laser ablation of Ni target in Au colloidal solution. *Mater. Chem. Phys.* **2015**, *166*, 223–232. [[CrossRef](#)]
47. Reboul, J.; Li, Z.Y.; Yuan, J.; Nakatsuka, K.; Saito, M.; Mori, K.; Yamashita, H.; Xia, Y.; Louis, C. Synthesis of small Ni-core-Au-shell catalytic nanoparticles on TiO₂ by galvanic replacement reaction. *Nanoscale Adv.* **2021**, *3*, 823–835. [[CrossRef](#)]
48. Liu, L.; Tai, X.; Zhou, X.; Hou, J.; Zhang, Z. Bimetallic Au-Ni alloy nanoparticles in a metal-organic framework (MIL-101) as efficient heterogeneous catalysts for selective oxidation of benzyl alcohol into benzaldehyde. *J. Alloys Compd.* **2019**, *790*, 326–336. [[CrossRef](#)]
49. Alotaibi, M.A.; Din, I.U.; Alharthi, A.I.; Bakht, M.; Centi, G.; Shaharun, M.S.; Naeem, A. Green methanol synthesis by catalytic CO₂ hydrogenation, deciphering the role of metal-metal interaction. *Sustain. Chem. Pharm.* **2021**, *21*, 100420. [[CrossRef](#)]
50. Jiao, J.; Fu, J.; Wei, Y.; Zhao, Z.; Duan, A.; Xu, C.; Li, J.; Song, H.; Zheng, P.; Wang, X.; et al. Al-modified dendritic mesoporous silica nanospheres-supported NiMo catalysts for the hydrodesulfurization of dibenzothiophene: Efficient accessibility of active sites and suitable metal-support interaction. *J. Catal.* **2017**, *356*, 269–282. [[CrossRef](#)]
51. Dan, M.; Mihet, M.; Tasnadi-Asztalos, Z.; Imre-Lucaci, A.; Katona, G.; Lazar, M.D. Hydrogen production by ethanol steam reforming on nickel catalysts: Effect of support modification by CeO₂ and La₂O₃. *Fuel* **2015**, *147*, 260–268. [[CrossRef](#)]
52. Velu, S.; Gangwal, S. Synthesis of alumina supported nickel nanoparticle catalysts and evaluation of nickel metal dispersions by temperature programmed desorption. *Solid State Ion.* **2006**, *177*, 803–811. [[CrossRef](#)]
53. Guerra-Que, Z.; Torres, J.G.T.; Vidal, H.P.; Cuauhtémoc, I.; Monteros, A.E.D.L.; Beltramini, J.; Frías-Márquez, D.M. Silver nanoparticles supported on zirconia-ceria for the catalytic wet air oxidation of methyl tert-butyl ether. *RSC Adv.* **2017**, *7*, 3599–3610. [[CrossRef](#)]
54. Guerra-Que, Z.; Pérez-Vidal, H.; Torres-Torres, G.; Arévalo-Pérez, J.C.; Pavón, A.A.S.; Cervantes-Urbe, A.; Monteros, A.E.D.L.; Lunagómez-Rocha, M.A. Treatment of phenol by catalytic wet air oxidation: A comparative study of copper and nickel supported on γ -alumina, ceria and γ -alumina-ceria. *RSC Adv.* **2019**, *9*, 8463–8479. [[CrossRef](#)]
55. Zhao, B.; Chen, Z.; Chen, Y.; Ma, X. Syngas methanation over Ni/SiO₂ catalyst prepared by ammonia-assisted impregnation. *Int. J. Hydrogen Energy* **2017**, *42*, 27073–27083. [[CrossRef](#)]
56. Shimizu, K.-I.; Kawachi, H.; Komai, S.-I.; Yoshida, K.; Sasaki, Y.; Satsuma, A. Carbon oxidation with Ag/ceria prepared by self-dispersion of Ag powder into nano-particles. *Catal. Today* **2011**, *175*, 93–99. [[CrossRef](#)]
57. Reddy, B.M.; Rao, K.N. Copper promoted ceria-zirconia based bimetallic catalysts for low temperature soot oxidation. *Catal. Commun.* **2009**, *10*, 1350–1353. [[CrossRef](#)]
58. Yang, S.; Besson, M.; Descorme, C. Catalytic wet air oxidation of succinic acid over Ru and Pt catalysts supported on Ce_xZr_{1-x}O₂ mixed oxides. *Appl. Catal. B Environ.* **2015**, *165*, 1–9. [[CrossRef](#)]
59. Wang, J.; Zhu, W.; He, X.; Yang, S. Catalytic wet air oxidation of acetic acid over different ruthenium catalysts. *Catal. Commun.* **2008**, *9*, 2163–2167. [[CrossRef](#)]

60. Tao, F.; Yang, S.; Yang, P.; Shi, Z.; Zhou, R. Effects of support property on the catalytic performance of CeO₂-ZrO₂-CrO_x for 1,2-dichloroethane oxidation. *J. Rare Earths* **2016**, *34*, 381–389. [[CrossRef](#)]
61. Parvas, M.; Haghighi, M.; Allahyari, S. Catalytic wet air oxidation of phenol over ultrasound-assisted synthesized Ni/CeO₂-ZrO₂ nanocatalyst used in wastewater treatment. *Arab. J. Chem.* **2019**, *12*, 1298–1307. [[CrossRef](#)]
62. Fu, H.; Leitner, N.K.V.; Legube, B. Catalytic ozonation of chlorinated carboxylic acids with Ru/CeO₂-TiO₂ catalyst in the aqueous system. *New J. Chem.* **2002**, *26*, 1662–1666. [[CrossRef](#)]
63. Chen, F.; Ho, P.; Ran, R.; Chen, W.; Si, Z.; Wu, X.; Weng, D.; Huang, Z.; Lee, C. Synergistic effect of CeO₂ modified TiO₂ photocatalyst on the enhancement of visible light photocatalytic performance. *J. Alloys Compd.* **2017**, *714*, 560–566. [[CrossRef](#)]
64. Tomova, D.; Iliev, V.; Eliyas, A.; Rakovsky, S. Promoting the oxidative removal rate of oxalic acid on gold-doped CeO₂/TiO₂ photocatalysts under UV and visible light irradiation. *Sep. Purif. Technol.* **2015**, *156*, 715–723. [[CrossRef](#)]
65. Fukumura, T.; Sambandan, E.; Yamashita, H. Synthesis and VOC degradation ability of a CeO₂/WO₃ thin-layer visible-light photocatalyst. *Mater. Res. Bull.* **2017**, *94*, 493–499. [[CrossRef](#)]
66. Roy, S.; Saroha, A.K. Ceria promoted γ -Al₂O₃ supported platinum catalyst for catalytic wet air oxidation of oxalic acid: Kinetics and catalyst deactivation. *RSC Adv.* **2014**, *4*, 56838–56847. [[CrossRef](#)]
67. Mahofa, E.P.; Narsaiah, T.B.; Chakra, C.S.; Kumar, P. Catalytic removal of soot from diesel engines using CeO₂, CeO₂-CuO₂, and CeO₂-Al₂O₃ nanocomposites. *Mater. Today Proc.* **2015**, *2*, 4451–4456. [[CrossRef](#)]
68. Guo, X.; Li, Y.-Y.; Shen, D.-H.; Gan, J.; Tian, M.; Liu, Z.-G. Metalloporphyrins immobilized on core-shell CeO₂@SiO₂ nanoparticles prepared by a double-coating method for oxidation of diphenyl methane. *Appl. Catal. A Gen.* **2012**, *413–414*, 30–35. [[CrossRef](#)]
69. Phanichphant, S.; Nakaruk, A.; Chaneei, D. Photocatalytic activity of the binary composite CeO₂/SiO₂ for degradation of dye. *Appl. Surf. Sci.* **2016**, *387*, 214–220. [[CrossRef](#)]
70. Punde, S.S.; Tatarchuk, B.J. Pt-CeO₂/SiO₂ catalyst for CO oxidation in humid air at ambient temperature. *Chin. J. Catal.* **2017**, *38*, 475–488. [[CrossRef](#)]
71. Klein, M.; Nadolna, J.; Golabiewska, A.; Mazierski, P.; Klimczuk, T.; Remita, H.; Zaleska-Medynska, A. The effect of metal cluster deposition route on structure and photocatalytic activity of mono- and bimetallic nanoparticles supported on TiO₂ by radiolytic method. *Appl. Surf. Sci.* **2016**, *378*, 37–48. [[CrossRef](#)]
72. Gong, P.; Xie, J.; Fang, D.; Liu, X.; He, F.; Li, F. Novel heterogeneous denitrification catalyst over a wide temperature range: Synergy between CeO₂, ZrO₂ and TiO₂. *Chem. Eng. J.* **2019**, *356*, 598–608. [[CrossRef](#)]
73. Lunagómez-Rocha, M.A.; Del Ángel, G.; Torres-Torres, G.; Cervantes, A.; Vázquez, A.; Arrieta, A.; Beltramini, J.N. Effect of the Pt oxidation state and Ce₃₊/Ce₄₊ ratio on the Pt/TiO₂-CeO₂ catalysts in the phenol degradation by catalytic wet air oxidation (CWAO). *Catal. Today* **2015**, *250*, 145–154. [[CrossRef](#)]
74. Monteros, A.E.D.L.; Lafaye, G.; Cervantes, A.; Del Angel, G.; Barbier, J., Jr.; Torres, J.G.T. Catalytic wet air oxidation of phenol over metal catalyst (Ru,Pt) supported on TiO₂-CeO₂ oxides. *Catal. Today* **2015**, *258*, 564–569. [[CrossRef](#)]
75. Izquierdo-Colorado, A.; Torres-Torres, G.; Gamboa-Rodríguez, M.T.; Silahua-Pavón, A.A.; Arévalo-Pérez, J.C.; Cervantes-Uribe, A.; Cordero-García, A.; Beltramini, J.N. Catalytic wet air oxidation (CWAO) of phenol in a fixed bed reactor using supported Ru and Ru-Au catalysts: Effect of gold and Ce loading. *ChemistrySelect* **2019**, *4*, 1275–1284. [[CrossRef](#)]
76. García-Hernández, L.E.; Frías-Márquez, D.M.; Pacheco-Sosa, J.G.; Cervantes-Uribe, A.; Arévalo-Pérez, J.C.; Pérez-Vidal, H.; Silahua-Pavón, A.A.; Lunagómez-Rocha, M.A.; Torres-Torres, J.G. 2-Chlorophenol degradation by catalytic wet air oxidation using copper supported on TiO₂-CeO₂-ZrO₂. *Water Sci. Technol.* **2019**, *80*, 911–919. [[CrossRef](#)] [[PubMed](#)]
77. Córdova-Pérez, G.E.; Torres-Torres, G.; Ortiz-Chi, F.; Godavarthi, S.; Silahua-Pavón, A.A.; Izquierdo-Colorado, A.; Da Costa, P.; Hernández-Como, N.; Alemán, M.; Espinosa-González, C.F. Effect of acid-basic sites ratio on the catalytic activity to obtain 5-HMF from glucose using Al₂O₃-TiO₂-W catalysts. *ChemistrySelect* **2018**, *3*, 12854–12864. [[CrossRef](#)]
78. Atanda, L.; Silahua, A.; Mukundan, S.; Shrotri, A.; Torres, J.G.T.; Beltramini, J. Catalytic behaviour of TiO₂-ZrO₂ binary oxide synthesized by sol-gel process for glucose conversion to 5-hydroxymethylfurfural. *RSC Adv.* **2015**, *5*, 80346–80352. [[CrossRef](#)]
79. Silahua-Pavón, A.A.; Espinosa-González, C.G.; Ortiz-Chi, F.; Pacheco-Sosa, J.G.; Pérez-Vidal, H.; Arévalo-Pérez, J.C.; Godavarthi, S.; Torres-Torres, J.G. Production of 5-HMF from glucose using TiO₂-ZrO₂ catalysts: Effect of the sol-gel synthesis additive. *Catal. Commun.* **2019**, *129*, 105723. [[CrossRef](#)]
80. Zhang, Y.; Zhou, Y.; Peng, C.; Shi, J.; Wang, Q.; He, L.; Shi, L. Enhanced activity and stability of copper oxide/ γ -alumina catalyst in catalytic wet-air oxidation: Critical roles of cerium incorporation. *Appl. Surf. Sci.* **2018**, *436*, 981–988. [[CrossRef](#)]
81. Li, N.; Descorme, C.; Besson, M. Catalytic wet air oxidation of 2-chlorophenol over Ru loaded Ce_xZr_{1-x}O₂ solid solutions. *Appl. Catal. B Environ.* **2007**, *76*, 92–100. [[CrossRef](#)]
82. Barbierjr, J.; Delanoë, F.; Jabouille, F.; Duprez, D.; Blanchard, G.; Isnard, P. Total oxidation of acetic acid in aqueous solutions over noble metal catalysts. *J. Catal.* **1998**, *177*, 378–385. [[CrossRef](#)]
83. Kundakovic, L.; Flytzani-Stephanopoulos, M. Cu- and Ag-modified cerium oxide catalysts for methane oxidation. *J. Catal.* **1998**, *179*, 203–221. [[CrossRef](#)]
84. Arena, F.; Italiano, C.; Raneri, A.; Saja, C. Mechanistic and kinetic insights into the wet air oxidation of phenol with oxygen (CWAO) by homogeneous and heterogeneous transition-metal catalysts. *Appl. Catal. B Environ.* **2010**, *99*, 321–328. [[CrossRef](#)]
85. Vittenet, J.; Aboussaoud, W.; Mendret, J.; Pic, J.-S.; Debellefontaine, H.; Lesage, N.; Faucher, K.; Manero, M.-H.; Thibault-Starzyk, F.; Leclerc, H.; et al. Brosillon, catalytic ozonation with γ -Al₂O₃ to enhance the degradation of refractory organics in water. *Appl. Catal. A Gen.* **2015**, *504*, 519–532. [[CrossRef](#)]

-
86. Massa, A.; Hernández, S.; Ansaloni, S.; Castellino, M.; Russo, N.; Fino, D. Enhanced electrochemical oxidation of phenol over manganese oxides under mild wet air oxidation conditions. *Electrochim. Acta* **2018**, *273*, 53–62. [[CrossRef](#)]
 87. Zhou, S.; Qian, Z.; Sun, T.; Xu, J.; Xia, C. Catalytic wet peroxide oxidation of phenol over Cu-Ni-Al hydrotalcite. *Appl. Clay Sci.* **2011**, *53*, 627–633. [[CrossRef](#)]
 88. Keav, S.; de los Monteros, A.E.; Barbier, J.; Duprez, D. Wet air oxidation of phenol over Pt and Ru catalysts supported on cerium-based oxides: Resistance to fouling and kinetic modelling. *Appl. Catal. B Environ.* **2014**, *150–151*, 402–410. [[CrossRef](#)]